Research Article

ADVANCED PHOTONICS

Observing the collapse of super-Bloch oscillations in strong-driving photonic temporal lattices

Xinyuan Hu,[a,†] Shulin Wang,[a,†] Chengzhi Qin,[a,*] Chenyu Liu,[a] Lange Zhao,[a] Yinglan Li,[a] Han Ye,[a] Weiwei Liu,[a,b] Stefano Longhi,[c,d,*] Peixiang Lu,[a,b,*] and Bing Wang[a,*]

[a]Huazhong University of Science and Technology, School of Physics, Wuhan National Laboratory for Optoelectronics, Wuhan, China
[b]Wuhan Institute of Technology, Hubei Key Laboratory of Optical Information and Pattern Recognition, Wuhan, China
[c]Politecnico di Milano, Dipartimento di Fisica, Milano, Italy
[d]IFISC (UIB-CSIC), Instituto de Fisica Interdisciplinary Sistemas Complejos, Palma de Mallorca, Spain

Abstract. Super-Bloch oscillations (SBOs) are amplified versions of direct current (dc)-driving Bloch oscillations realized under the detuned dc- and alternating current (ac)-driving electric fields. A unique feature of SBOs is the coherent oscillation inhibition via the ac-driving renormalization effect, which is dubbed as the collapse of SBOs. However, previous experimental studies on SBOs have only been limited to the weak ac-driving regime, and the collapse of SBOs has not been observed. Here, by harnessing a synthetic temporal lattice in fiber-loop systems, we push the ac-field into a strong-driving regime and observe the collapse of SBOs, which manifests as the oscillation-trajectory localization at specific ac-driving amplitudes and oscillation-direction flip by crossing collapse points. By adopting arbitrary-wave ac-driving fields, we also realize generalized SBOs with engineered collapse conditions. Finally, we exploit the oscillation-direction flip features to design tunable temporal beam routers and splitters. We initiate and demonstrate the collapse of SBOs, which may feature applications in coherent wave localization control for optical communications and signal processing.

Keywords: super-Bloch oscillations; band collapse; ac-driving renormalization effect; photonic temporal lattices; strong-driving regime.

Received Mar. 8, 2024; revised manuscript received Apr. 29, 2024; accepted for publication Jun. 3, 2024; published online Jul. 2, 2024.

[DOI: 10.1117/1.AP.6.4.046001]

1 Introduction

Quantum-charged particles such as electrons display a wide variety of coherent transport effects under the action of external electric fields.[1–3] For example, in the absence of dephasing and collisional effects, the electrons in the solids exposed to a direct current (dc) electric field tend to experience periodic oscillation rather than directional transport, which is now known as the famous Bloch oscillations (BOs).[4–6] Despite being predicted one century ago, experimental demonstrations of BOs remained elusive for a long time, owing to the dephasing and collisional effects in solid-state crystals that overwhelm coherent electron motion. It was only quite recently that BOs have been experimentally observed in clean or synthetic matter systems with long coherence times, such as superlattices, ultracold atoms in optical lattices, and photonic waveguide lattices.[4–6]

Super-Bloch oscillations (SBOs), the giant oscillatory motions under the action of detuned dc- and alternating current (ac)-driving electric fields, have emerged as the amplified versions of BOs.[7–23] The unique feature of SBOs is that their oscillation amplitude can be modified by the ac-driving amplitude through a renormalized factor, which has no direct counterpart in BOs and provides more powerful degrees of freedom for

*Address all correspondence to Chengzhi Qin, qinchengzhi@hust.edu.cn; Stefano Longhi, stefano.longhi@polimi.it; Peixiang Lu, lupeixiang@hust.edu.cn; Bing Wang, wangbing@hust.edu.cn

†These authors contributed equally to this work.

coherent oscillation control. For example, for the simplest sinusoidal ac-driving case,[7–23] the renormalized factor takes the Bessel function. In this case, when the ac-driving amplitude takes each root of the Bessel function, the oscillation amplitude will vanish, which is accompanied by the flip of the initial oscillation direction. This interesting phenomenon is dubbed as the collapse of SBOs, which is typically achieved in the strong ac-driving regime. As compared to ordinary BOs, SBOs have drawn little attention mainly because their experimental observation is more challenging and requires a much longer coherence time. To date, SBOs have only been demonstrated in cold-atomic systems.[10,17] However, in these studies, since only a weak ac-driving field was applied, the interesting phenomenon of SBO collapse occurring in the strong-driving regime was not observed. Moreover, all present theoretical and experimental studies on SBOs have been limited to the simplest sinusoidal ac-driving cases.[7–23] The fate of SBO collapse under more general ac-driving formats and the ability of harnessing SBOs for flexible coherent wave packet manipulation remain so far unexplored.

In this work, by utilizing a synthetic temporal lattice based on a coupled fiber-loop circuit, we can synthesize an ac-driving field with arbitrary value and successfully achieve the collapse of SBOs in the strong-driving regime. The concept of photonic synthetic dimensions has sparked a surge of interest in recent years, with typical examples, including the frequency,[24–29] time,[30–44] and orbital angular momentum lattices.[45–47] Among others, synthetic temporal lattices created from two coupled fiber loops have drawn extensive attention due to their advantages in introducing and controlling effective gauge fields therein through external modulations. A plethora of discrete-wave phenomena that are difficult to realize in the spatial lattices have been observed in these temporal lattices, ranging from parity-time symmetry,[37] non-Hermitian skin effect,[38,48] to the measurement of Berry curvature.[36] In particular, a variety of electric-field-driving effects have also been demonstrated based on this platform, including dc-driving BOs,[30,32] ac-driving dynamic localizations,[40,43] and Landau–Zener tunneling.[44] Here, by combining both a dc-driving and a nearly detuned ac-driving electric field in the synthetic temporal lattice, we successfully achieve SBOs up into the strong-driving regime. Particularly, in this regime, we observe the features of vanishing oscillation amplitude and a flip of initial oscillation direction at specific driving amplitudes, showing the clear signatures of SBO collapse. The characteristic rapid swing features of SBOs and the collapse of SBOs have also been analyzed from the Fourier spectrum of oscillation patterns. By generalizing SBOs from the sinusoidal driving to an arbitrary-wave driving format, we also observe the generalized SBOs with tunable collapse conditions. Finally, we exploit the oscillation direction flip feature to design tunable temporal beam routers and splitters. The study may find applications in temporal pulse reshaping and coherent oscillation control used for optical communications and signal processing.

2 Results and Discussion

2.1 Theoretical Model of SBOs in Photonic Temporal Lattices

The synthetic temporal lattice is constructed by mapping from the pulse evolution in two coupled fiber loops,[30–44] as shown schematically in Figs. 1(a) and 1(b). Here, the pulse circulation in the short/long loops corresponds to the leftward/rightward

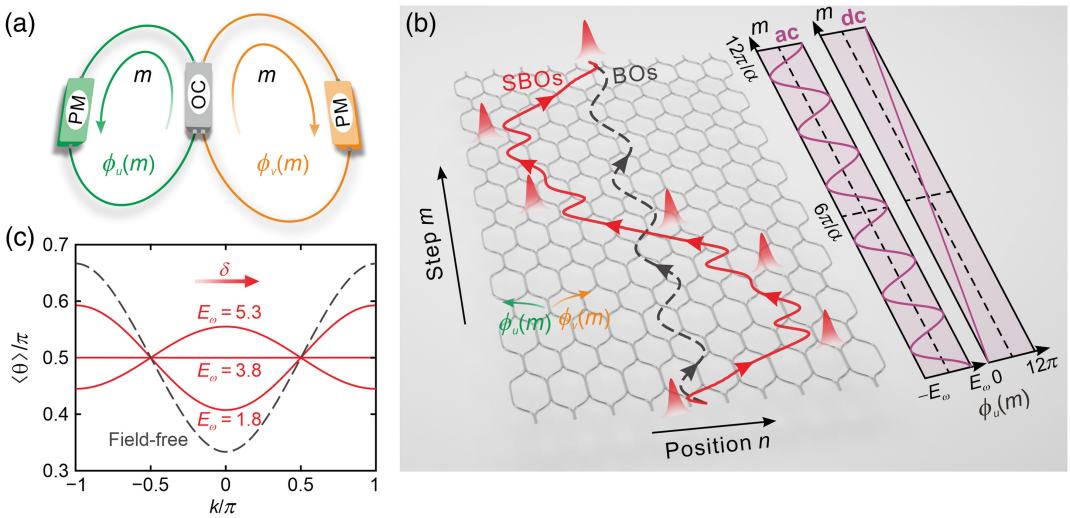

Fig. 1 Principle of SBOs in electric-field-driven synthetic temporal lattices. (a) Two fiber loops with slightly different lengths are connected by an OC to construct the temporal lattice. The incorporated PMs in the short and long loops can introduce the step-dependent phase shifts of $\phi_u(m)$ and $\phi_v(m)$. (b) Schematic of the synthetic temporal lattice mapped from the pulse evolution in two coupled fiber loops in panel (a) and the sketch of SBO trajectory denoted by the red curve. The purple curves denote the required dc- and ac-driving electric fields to induce SBOs, which are created simultaneously by imposing opposite phase shifts of $\phi_u(m)$ and $\phi_v(m)$ in short and long loops. (c) Effective time-averaging band structure of the synthetic temporal lattice at $E_\omega = 1.8$, 3.8, and 5.3. The dashed curve is the original band structure without electric-field driving, where δ is the frequency detuning between the dc- and ac-driving electric field.

hopping in the links, and pulse interference at the central coupler is associated with light scattering at each node in the lattice. Then, the circulation times and pulse relative positions can be mapped into the longitudinal evolution step "m" and transverse lattice site n. By further incorporating phase modulators (PMs) into the two loops, we can introduce the additional phase shifts of $\phi_u(m)$ and $\phi_v(m)$ along the leftward and rightward paths. The pulse dynamics in the lattice is governed by the following coupled-mode equations:

$$\begin{cases} u_n^{m+1} = [\cos(\beta)u_{n+1}^m + i\sin(\beta)v_{n+1}^m]e^{i\phi_u(m)}, \\ v_n^{m+1} = [i\sin(\beta)u_{n-1}^m + \cos(\beta)v_{n-1}^m]e^{i\phi_v(m)}, \end{cases} \tag{1}$$

where u_n^m and v_n^m represent the complex amplitudes of pulses in the short and long loops, and $\sin^2(\beta)/\cos^2(\beta)$ is the splitting ratio of the central optical coupler (OC) with $\beta \in [0, \pi/2]$. In the absence of the phase shifts, the eigen Bloch mode supported in the lattice is $(u_n^m, v_n^m)^T = (U, V)^T \exp(ikn)\exp(i\theta m)$, where $(U, V)^T$ is the eigenvector and k and θ are the transverse Bloch momentum and longitudinal propagation constant, respectively. By plugging the Bloch mode into Eq. (1), we can obtain the band structure $\theta_\pm(k) = \pm\arccos[\cos(\beta)\cos(k)]$, where "$\pm$" denotes upper and lower bands. Usually for $\beta \to \pi/2$, by applying Taylor expansion and ignoring high-order terms, we can obtain the approximated band structure,[37,42,43]

$$\theta_\pm(k) = \pm\cos(\beta)\cos(k) \mp \frac{\pi}{2}. \tag{2}$$

To induce SBOs, we need to apply simultaneously a detuned dc and ac electric field in the lattice, $E_{\text{eff}}(m) = \alpha + E_{\text{ac}}\sin(\omega_{\text{ac}}m + \varphi)$, where α is the magnitude of dc electric field, corresponding to the BO frequency $\omega_{\text{BOs}} = \alpha$, and E_{ac}, ω_{ac}, and φ are the driving amplitude, frequency, and initial phase of ac electric field, respectively. As the dc and ac fields satisfy the resonance condition (Stark resonance), $\alpha = N\omega_{\text{ac}}$, where N is an integer denoting the resonance order, the effect of directional transport rather than SBOs will occur. The packet will undergo aperiodic transport instead of periodic SBO motion in the lattice.[7,8] Under specific ac-driving amplitude satisfying $J_0(E_\omega) = 0$, destructive suppression of lattice's hopping occurs, leading to the dynamic localization effect, where $E_\omega = E_{\text{ac}}/\omega_{\text{ac}}$ is the normalized ac-driving amplitude denoting the amplitude-to-frequency ratio. Based on the resonance condition, SBOs can be further induced by introducing a slight detuning between the ac-driving and BO frequencies, i.e., $\alpha = N\omega_{\text{ac}} + \delta$, where δ is the frequency detuning. Under the dc and ac electric fields, the effective vector potential evolves as $A_{\text{eff}}(m) = -\int_0^m E_{\text{eff}}(m)\text{d}m = -\alpha m + E_\omega\cos(\omega_{ac}m + \varphi)$, which consists of a linearly varying and a sinusoidally oscillating term. In our synthetic mesh lattice, both dc and ac fields are simultaneously introduced by creating a time-varying vector potential $A_{\text{eff}}(m)$ by applying opposite phase modulations into the two fiber loops, $\phi_u(m) = -A_{\text{eff}}(m)$ and $\phi_v(m) = A_{\text{eff}}(m)$.[25,49,50] The vector potential is assumed to vary slowly with m, so that Zener tunneling between the two quasi-energy bands is negligible. Moreover, both ω_{ac} and α are assumed to be fractional integers than 2π to ensure periodicity of the dynamics after a full cycle. The instantaneous Bloch momentum is given by

$$k(m) = k - A_{\text{eff}}(m) = k + (N\omega_{\text{ac}} + \delta)m - E_\omega\cos(\omega_{\text{ac}}m + \varphi), \tag{3}$$

where k is the initial Bloch momentum. Usually, the frequency detuning δ is a very tiny quantity, which means that the high-frequency driving condition is always satisfied, i.e., $\omega_{\text{ac}} \gg \delta$. Under this condition, the instantaneous Bloch momentum evolves at two different time scales: a very rapid one induced by ω_{ac} and a slow one induced by δ, such that the term "δm" in Eq. (3) can be considered constant in one ac-driving period $M_{\text{ac}} = 2\pi/\omega_{\text{ac}}$. In the spirit of Magnus expansion, we can use a time-averaging band structure to approximate the rigorous band structure $\theta_\pm[k(m)]$ (see Note 1 in the Supplementary Material for derivation),

$$\begin{aligned} \langle\theta_\pm(k)\rangle &= \frac{1}{M_{\text{ac}}}\int_0^{M_{\text{ac}}}\theta_\pm[k(m)]\text{d}m \\ &= \mp J_N(E_\omega)\cos(\beta)\cos\left[k + \delta m - N\left(\varphi + \frac{\pi}{2}\right)\right] \mp \frac{\pi}{2}, \end{aligned} \tag{4}$$

where $J_N(E_\omega)$ is the Nth-order Bessel function of the first kind. By comparing it with Eq. (2), we can find that the physical effect of the ac-driving field on the effective band structure is to renormalize the width of the two bands by a renormalization factor $J_N(E_\omega)$. The effective band structures for several $E_\omega = 1.8$, 3.8, and 5.3 with $N = 1$, $\omega_{\text{ac}} = \pi/30$, and $\varphi = \pi/2$ are shown in Fig. 1(c). One can see that the band collapses to a totally flat band as E_ω is chosen as the root of $J_1(E_\omega)$, i.e., $E_\omega = 3.8$. As we will demonstrate below, this band collapse condition is just responsible for the collapse of SBOs.

From the effective band structure, we can further obtain the averaging group velocity for a Bloch-wave packet with a central Bloch momentum k,

$$\begin{aligned} \langle v_{\text{g},\pm}(k)\rangle &= -\frac{\partial\langle\theta_\pm(k)\rangle}{\partial k} \\ &= \mp J_N(E_\omega)\cos(\beta)\sin\left[k + \delta m - N\left(\varphi + \frac{\pi}{2}\right)\right]. \end{aligned} \tag{5}$$

During a long evolution time, i.e., with multiple ac-driving periods, the effect of frequency detuning δ is to make the Bloch momentum linearly sweep across the Brillouin zone, which is analogous to the role of dc field in the situation of BOs. Due to the periodic nature of the band structure, the linear sweeping of Bloch momentum will also induce periodic oscillation of the packet in the lattice, which is dubbed the effect of SBOs.[10,12] In particular, SBOs can be described as an oscillatory averaging trajectory of the packet's center of mass in the (n, m) plane,

$$\begin{aligned} \langle\Delta n_\pm(m)\rangle &= \int_0^{M_{\text{ac}}}\langle v_{\text{g},\pm}(k)\rangle\text{d}m \\ &= \pm\frac{J_N(E_\omega)\cos(\beta)}{\delta}\left\{\cos\left[\delta m + k - N\left(\varphi + \frac{\pi}{2}\right)\right]\right. \\ &\quad \left. - \cos\left[k - N\left(\varphi + \frac{\pi}{2}\right)\right]\right\}. \end{aligned} \tag{6}$$

In an analogy to BOs, SBOs also exhibit a cosine-shaped averaging oscillation trajectory

$$\langle\Delta n_\pm(m)\rangle = A_{\text{SBOs}}[\cos(\omega_{\text{SBOs}}m + \varphi_{\text{SBOs}}) - \cos(\varphi_{\text{SBOs}})], \tag{7}$$

where the oscillation amplitude, frequency (period), and initial phase are given by

$$A_{\mathrm{SBOs}} = |\frac{J_N(E_\omega)\cos(\beta)}{\delta}|, \tag{8a}$$

$$\omega_{\mathrm{SBOs}} = |\delta|,\ M_{\mathrm{SBOs}} = |\frac{2\pi}{\delta}|, \tag{8b}$$

$$\varphi_{\mathrm{SBOs},+} = k - N\left(\varphi + \frac{\pi}{2}\right), \tag{8c}$$

for the upper band and $\varphi_{\mathrm{SBOs},-} = \varphi_{\mathrm{SBOs},+} + \pi$ for the lower band. Similar to BOs where both the oscillation amplitude and period are inversely proportional to the dc-driving field, $A_{\mathrm{BOs}} = |\cos(\beta)/\alpha|, M_{\mathrm{BOs}} = |2\pi/\alpha|$, the oscillation amplitude and period of SBOs are both inversely proportional to frequency detuning δ. Since $|\delta| \ll |\alpha|$, SBOs exhibit much larger oscillation amplitude and longer oscillation period compared with those of BOs, manifesting themselves as very giant oscillatory motions. As indicated by Eqs. (8a) and (8b), both SBO oscillation amplitude A_{SBOs} and period M_{SBOs} increase as the frequency detuning $|\delta|$ decreases. In the limit case of a vanishing frequency detuning $|\delta| = 0$, both oscillation amplitude and period become divergent, i.e., $A_{\mathrm{SBOs}} = \infty, M_{\mathrm{SBOs}} = \infty$, where SBOs degrade into the directional transport effect realized as the Stark resonance condition is satisfied.[8,9] So the directional transport is the limit case of SBOs with divergent oscillation amplitude and period under vanishing detuning $|\delta| = 0$. In addition, the initial oscillation phase of SBOs is proportional to the incident Bloch momentum k, which is also determined by the resonant order N as well as the ac-driving phase φ, as described in Eq. (8c).

An essential difference between SBOs and BOs is that the oscillation amplitude of SBOs can be further modified by the ac-driving amplitude through the renormalization factor $J_N(E_\omega)$. Specifically, as E_ω takes each root of J_N function, the oscillation amplitude will vanish, $A_{\mathrm{SBOs}} = 0$, which is dubbed the collapse of SBOs. Note that at the collapse point, the effective band structure collapses into flat bands, as is clearly shown in Fig. 1(c). The presence of oscillation amplitude collapse is a clear signature of SBOs, which does not occur in BOs. Another interesting feature accompanying the collapse of SBOs is the change of the sign "$\pm$" for $\langle \Delta n_\pm(m)\rangle$ as E_ω passes the collapse point, which manifests as the flip of oscillation direction. In this sense, we can also control the initial oscillation direction by harnessing the collapse of SBOs.

Although the above analysis based on averaging oscillation trajectory $\langle \Delta n_\pm(m)\rangle$ can capture the main oscillation feature of SBOs, the more rapid swing oscillation details within one ac-driving period are lost. Also, for previous studies on SBOs in cold-atomic systems,[10,17] these rapid swing oscillation details have not been observed, mainly due to the limited time resolution in measurements. Here, our measurements can resolve the wave-packet dynamics at each explicit evolution step, which allows us to inspect these rapid swing oscillation details. In the following, we will study the oscillation details by checking the Fourier spectrum of the SBO trajectory. As we will show below, the occurrence of SBO collapse can also be probed from the information on the Fourier spectrum. With this aim, we start from the packet's instantaneous group velocity obtained from Eq. (2),

$$\begin{aligned} v_{\mathrm{g},\pm}(m) &= -\frac{\mathrm{d}\theta_\pm[k(m)]}{\mathrm{d}k} \\ &= \pm\cos(\beta)\sin[k + (N\omega_{\mathrm{ac}} + \delta)m \\ &\quad - E_\omega\cos(\omega_{\mathrm{ac}}m + \varphi)], \end{aligned} \tag{9}$$

from which we can obtain the rigorous, instantaneous oscillation trajectory $\Delta n_\pm(m) = \int_0^m v_{g,\pm}(m)\mathrm{d}m$, which consists of rapid oscillation details around the SBO trajectory, $\Delta n_\pm(m) = \langle \Delta n_\pm(m)\rangle + \Delta n_{\mathrm{swing}}(m)$. A more detailed analysis of the instantaneous group velocities and trajectories is present in Note 2 in the Supplementary Material. In terms of Fourier analysis, the spectrum of rigorous oscillation trajectory can be decomposed into the superposition of the SBO frequency ω_{SBOs} and a continuum of higher swing spectrum components,

$$\begin{aligned} \Delta n_\pm(m) &= \int_0^{+\infty} A(\omega)\cos(\omega m + \varphi_\omega)\mathrm{d}\omega, \\ &= A_{\mathrm{SBOs}}\cos(\omega_{\mathrm{SBOs}}m + \varphi_{\mathrm{SBOs}}) \\ &\quad + \int_{0,\omega\neq\omega_{\mathrm{SBOs}}}^{+\infty} A(\omega)\cos(\omega m + \varphi_\omega)\mathrm{d}\omega, \end{aligned} \tag{10}$$

where $A(\omega) = \mathcal{F}[\Delta n_{\mathrm{swing}}(m)]$ is the Fourier transform of the rapid swing trajectory. From the Fourier spectrum, we can further extract the ratio of the power spectrum for SBOs,

$$R_{\mathrm{SBOs}} = \frac{|A_{\mathrm{SBOs}}|^2}{\int_0^{+\infty}|A(\omega)|^2\mathrm{d}\omega}, \tag{11}$$

and $R_{\mathrm{swing}} = 1 - R_{\mathrm{SBOs}}$ for the swing spectrum components. Meanwhile, we adopt the standard deviation to estimate the spectrum distribution of swing components beyond α,

$$\sigma(\omega) = \sqrt{\frac{\int_\alpha^{+\infty}\omega^2|A(\omega)|^2\mathrm{d}\omega}{\int_0^{+\infty}|A(\omega)|^2\mathrm{d}\omega}}. \tag{12}$$

A larger standard deviation means that the spectrum contains more high-frequency swing components, indicating that SBOs contain more rapid swing oscillation details.

2.2 Experimental Realization of SBOs

To comprehensively study SBOs, we build two coupled fiber-loop experimental platforms, as shown in Fig. 2. The initial optical pulse is prepared from the 1555 nm continuous wave laser beam by passing it through a Mach–Zehnder modulator (MZM), which generates a pulse with a width of ~100 ns. Then, the pulse is injected into the long loop through an optical switch (OS) and circulated in the double-loop circuit by the central OC. To construct the artificial dc- and ac-driving electric field essential for the SBOs, the phase modulation $2\phi_u(m)$ is implemented into the short loop by a PM, corresponding to the opposite phase modulations $\pm\phi_u(m)$ in the two loops, as required in the previous text. The evolution of pulse-train intensity is recorded at each step with photodiodes (PDs) and oscilloscopes (OSCs) by coupling the circulating pulses out of the loops. In detail, the two loops have an average length of ~5 km and a length difference of ~30 m, and the coupling ratio of the central OC is fixed at 75:25, which corresponds to $\beta = \pi/3$. Specifically, the erbium-doped fiber amplifiers (EDFAs) are

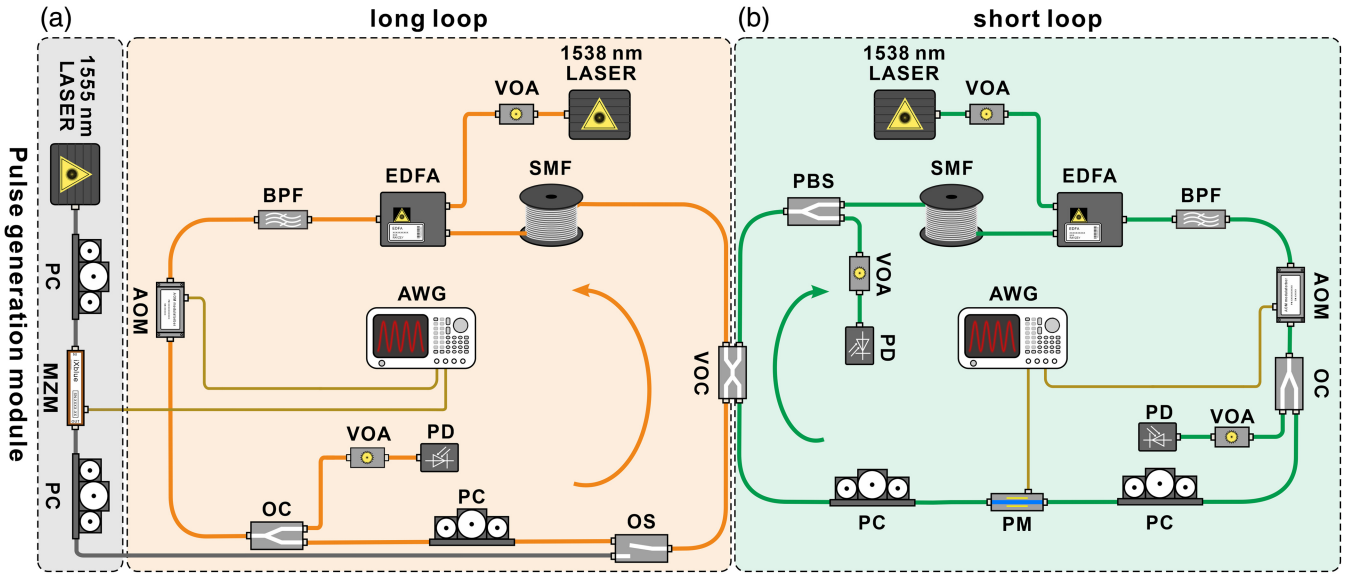

Fig. 2 Experimental setup. Panels (a) and (b) denote the long and short loops, respectively. All optical and electric components are as follows: PC, polarization controller; MZM, Mach–Zehnder modulator; OS, optical switch; OC, optical coupler; SMF, single-mode fiber; EDFA, erbium-doped fiber amplifier; VOA, variable optical attenuator; BPF, bandpass filter; AOM, acoustic optical modulator; PD, photodiode; OSC, oscilloscope; PBS, polarization beam splitter; PM, phase modulator; AWG, arbitrary waveform generator.

inserted in the two loops to compensate for losses during pulse circulation. To overcome the transient response noise, a high-power 1538 nm continuous-wave control light is introduced before the EDFA and a bandpass filter (BPF) is used after the EDFA to remove the control light and the spontaneous emission noise. In addition, the polarization controllers (PCs) and polarization beam splitter (PBS) are utilized to control the polarization states of pulses. The acoustic optical modulators (AOMs) serve as intensity modulators in the two loops, which can absorb the optical signals after hundreds of circulations. All modulators in our setup, including MZM, AOM, and PM, are driven by the AWGs, which can be flexibly controlled and reconfigured in real time and are advantageous for the synthesis of arbitrary driving waveforms to realize generalized SBOs.

Figure 3(a) shows the measured SBO oscillation amplitude A_{SBOs} as the function of the ac-driving amplitude E_ω and the inverse of frequency detuning $1/\delta$. The other parameters are chosen as $\omega_{\mathrm{ac}} = \pi/30$, $\varphi = \pi/2$, and $\alpha = N\omega_{\mathrm{ac}} + \delta$, where $N = 1$. The input Bloch wave packet is excited from the upper band with central carrier Bloch momentum $k = \pi/2$. To meet the high-frequency ac-driving condition, we choose $\delta = \pi/90$, $\pi/120$, and $\pi/150$ in our experiment, which satisfy $\omega_{\mathrm{ac}} = 3\delta - 5\delta$. For a fixed frequency detuning $\delta = \pi/150$, the oscillation amplitude A_{SBOs} increases in the weak-driving regime and decreases in the strong-driven regime, which precisely follows the $J_1(E_\omega)$ function, as given by the theoretical prediction in Eq. (8a). The measured packet intensity evolutions for four different ac-driving amplitudes $E_\omega = 1.8$, 3, 3.8, and 5.3 cases are shown in Figs. 3(d)–3(g), which possess $A_{\mathrm{SBOs}} = 14.3$, 8.2, 0, and 8.3. Note that for $E_\omega = 3.8$, i.e., the first root of $J_1(E_\omega)$ function is reached, the oscillation amplitude vanishes (denoted by green arrow), clearly showing the collapse of SBOs. On the other hand, for a fixed E_ω, we can get $A_{\mathrm{SBOs}} = 8.3$ for $\delta = \pi/150$ and $A_{\mathrm{SBOs}} = 4.9$ for $\delta = \pi/90$, as shown in Figs. 3(g) and 3(h), also verifying the inverse dependence of A_{SBOs} on δ as given in Eq. (8a). The oscillation period M_{SBOs} versus $1/\delta$ is depicted in Fig. 3(b), which is also inversely proportional to δ described in Eq. (8b). This inverse dependence law can also be evidenced in Figs. 3(g) and 3(h), which show $M_{\mathrm{SBOs}} = 289$ for $\delta = \pi/150$ and $M_{\mathrm{SBOs}} = 178$ for $\delta = \pi/90$.

Then, we experimentally study the initial oscillation phase of SBOs. Figure 3(c) shows the initial oscillation phases φ_{SBOs} versus the incident Bloch momentum k for two different ac-driving amplitudes $E_\omega = 1.8$ and 5.3 between the collapse points. The oscillation phases show linear dependences on k, i.e., $\varphi_{\mathrm{SBOs}} = k - \pi$ by choosing $N = 1$ and $\varphi = \pi/2$, also in agreement with the theoretical analysis in Eq. (8c). Note that there is a flip of oscillation direction as a π-phase jump as E_ω crosses the SBO collapse point, which is the direct consequence of sign change of $J_1(E_\omega)$ function. This π-phase jump feature can also be verified by the field evolutions in Figs. 3(d) and 3(g), which show opposite initial oscillation directions with $\varphi_{\mathrm{SBOs}} = -0.47\pi$ and -0.03π for $k = \pi/2$ under $E_\omega = 1.8$ and 5.3, respectively.

Next, we investigate the rapid swing oscillation details by calculating the Fourier spectrum of the measured packet's oscillation trajectory. Figure 4(a) shows the power ratio R_{SBOs} of SBO frequency ω_{SBOs} relative to all spectrum components as a function of the ac-driving amplitude. One can see a dip in the ratio $R_{\mathrm{SBOs}} = 0$ for $E_\omega = 3.8$, showing the clear signature of the occurrence of SBO collapse. By contrast, as $E_\omega = 3.8$ is chosen far away from the collapse point, such as for $E_\omega = 1.8$ and $E_\omega = 5.3$, R_{SBOs} approaches unity, meaning that SBOs are dominated by the slowly varying averaging trajectory and that the portion of rapid swing details is very tiny. Figure 4(b) shows the standard deviation $\sigma(\omega)$ of the Fourier spectrum for the rapid swing frequency components, which manifests as a monotonical increase with E_ω, indicating that the presence of SBO collapse does not influence the spectral distribution for the fast-swing

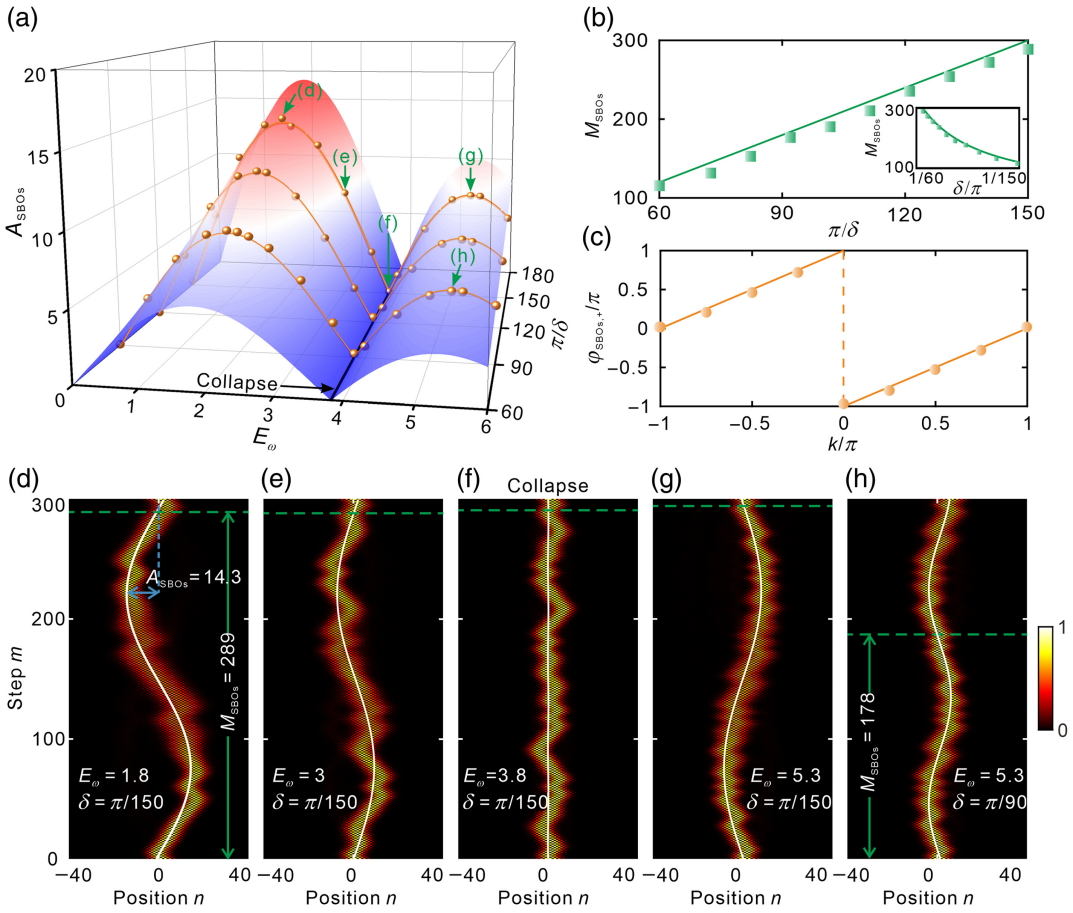

Fig. 3 Simulated and measured results of SBOs. (a) SBO oscillation amplitude A_{SBOs} as a function of the ac-driving amplitude E_ω and the inverse frequency detuning $1/\delta$. The golden spheres represent the measured results. (b) SBO oscillation period M_{SBOs} as a function of the inverse frequency detuning $1/\delta$. The curve and squares denote the calculated and measured results, respectively. The inset figure shows M_{SBOs} as a function of δ. (c) Initial oscillation phase of SBOs versus the initial Bloch momentum k for $E_\omega = 1.8$, $N = 1$, $\varphi = \pi/2$, and $\delta = \pi/150$. The solid curves and spheres denote the theoretical and experimental results, respectively. (d)–(g) Measured pulse intensity evolutions for $E_\omega = 1.8$, 3, 3.8, and 5.3 under $\delta = \pi/150$. The white solid curves denote the averaging SBO oscillation trajectories $\langle \Delta n_\pm(m) \rangle$ obtained by fitting from the experimental results using the cosine function. The blue and green lines denote the SBO oscillation amplitude A_{SBOs} and period M_{SBOs}, respectively. (h) Experimental pulse intensity evolution for $E_\omega = 5.3$ and $\delta = \pi/90$.

frequency components. Figures 4(c)–4(e) show the corresponding Fourier spectra for the measured SBO trajectories for $E_\omega = 1.8$, 3.8, and 5.3. We can find that the peak at $\omega = \omega_{SBOs}$ disappears in the spectrum for $E_\omega = 3.8$, which can further validate the occurrence of the collapse of SBOs, while for $E_\omega = 1.8$ and 5.3, the spectrum reaches the maximum at $\omega = \omega_{SBOs}$, meaning that the SBOs dominate by choosing far away from the SBO collapse point.

2.3 Generalized SBOs under an Arbitrary-Wave ac-Driving Field

While all previous studies on SBOs have been focused on the simplest sinusoidal ac-driving case, here we will show that SBOs can still persist even under an arbitrary-wave ac-driving field, which is dubbed generalized SBOs. Interestingly, generalized SBOs manifest different renormalization factors in the oscillation amplitude compared with the Bessel function factor for the sinusoidal driving case, which will lead to different collapse conditions. Below, we will choose two exemplified arbitrary-wave ac-driving fields with rectangular and triangular waveforms for experimental demonstrations.

For rectangular wave driving, the waveform in one ac-driving period $m \in [0, M_{ac}]$ is given by

$$E_{\text{eff}}(m) = \begin{cases} E_{\text{ac}}, & m \in [0, M_{\text{ac}}/2) \\ -E_{\text{ac}}, & m \in [M_{\text{ac}}/2, M_{\text{ac}}) \end{cases}. \tag{13}$$

By applying similar procedures to the sinusoidal driving case in Eqs. (3)–(6), we can also calculate the time-averaging trajectory for the generalized SBOs (see Note 3 in the Supplementary Material, for detailed derivation),

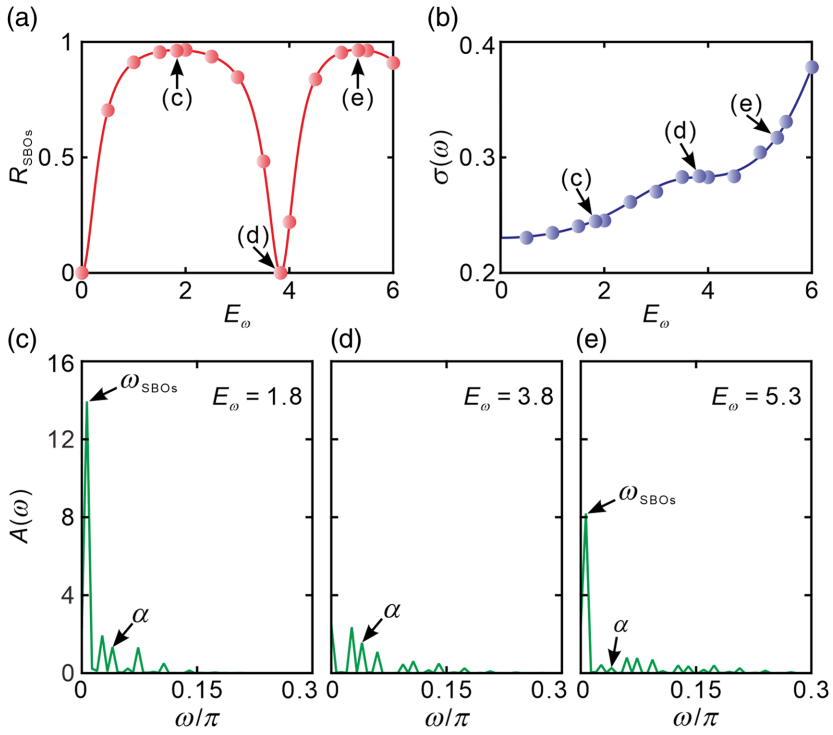

Fig. 4 Fourier spectrum of SBOs. (a) The power ratio of SBOs with respect to all Fourier spectrum components as a function of the ac-driving amplitude E_ω. The solid curve and spheres denote the theoretical and experimental results, respectively. (b) The standard deviation of the Fourier spectrum for $\omega > \alpha$ varying with E_ω. (c)–(e) Fourier spectra of measured SBO trajectories at $E_\omega = 1.8$, 3.8, and 5.3.

$$\langle \Delta n_{\pm}(m) \rangle = \pm \frac{f(E_\omega)\cos(\beta)}{\delta}[\cos(\delta m + k) - \cos(k)], \tag{14}$$

where the renormalization factor is given by

$$f(E_\omega) = \frac{2E_\omega \sin[\pi(E_\omega + N)/2]}{\pi(E_\omega + N)(E_\omega - N)}. \tag{15}$$

Similarly, for a triangular-waveform driving

$$E_{\text{eff}}(m) = \begin{cases} E_{\text{ac}} - 4E_{\text{ac}} m/M_{\text{ac}}, & m \in [0, M_{\text{ac}}/2) \\ -E_{\text{ac}} + 4E_{\text{ac}}(m - M_{\text{ac}}/2)/M_{\text{ac}}, & m \in [M_{\text{ac}}/2, M_{\text{ac}}) \end{cases}, \tag{16}$$

we can also obtain a generic averaging oscillation trajectory of Eq. (14), with only $f(E_\omega)$ replaced by

$$f(E_\omega) = \sqrt{\frac{1}{2E_\omega}}\left\{\cos(x)[C(x_+) + C(x_-)] - \sin(x)[S(x_+) + S(x_-)]\right\}, \tag{17}$$

where $C(x) = \int_0^x \cos(t^2)\mathrm{d}t$ and $S(x) = \int_0^x \sin(t^2)\mathrm{d}t$ are Fresnel integrals, $x = \pi E_\omega/4 + N\pi/2 + N^2\pi/(4E_\omega)$, and $x_\pm = (E_\omega/2)^{1/2} \pm (N^2/2E_\omega)^{1/2}$. For the two cases, the oscillation amplitude, frequency (period), and initial phase can be extracted from Eq. (14),

$$A_{\text{SBOs}} = \left|\frac{f(E_\omega)\cos(\beta)}{\delta}\right|, \tag{18a}$$

$$\omega_{\text{SBOs}} = |\delta|,\ M_{\text{SBOs}} = \left|\frac{2\pi}{\delta}\right|, \tag{18b}$$

$$\varphi_{\text{SBOs},+} = k. \tag{18c}$$

By comparing Eqs. (18a)–(18c) with the sinusoidal-wave driving case in Eqs. (8a)–(8c), we can find that applying different driving waveforms does not change the oscillation frequency of SBOs but can modify the oscillation amplitude via a generic renormalization factor $f(E_\omega)$, which are given by $J_N(E_\omega)$ and Eqs. (15) and (17) for the three waveforms. Meanwhile, the initial oscillation phase is still proportional to the incident Bloch momentum k. Likewise, as the driving amplitude E_ω takes the roots of the $f(E_\omega)$ function, the oscillation amplitude will also vanish, which can be referred to as the collapse of generalized SBOs. In particular, for rectangular-wave driving, to achieve $f(E_\omega) = 0$, one requires $\pi(E_\omega + N)/2 = p\pi$ (p is an integer) and $E_\omega - N \neq 0$, which leads to $E_\omega = 2p - N$, and $p \neq N$. For example, for $N = 1$, the collapse of SBOs occurs at an odd value of $E_\omega = 2p - 1 = 3, 5, \ldots$, etc.

The theoretical analysis has also been verified by our experiments. Figure 5(b) shows the measured A_{SBOs} versus E_ω under the three driving waveforms, all of which can vanish with $A_{\text{SBOs}} = 0$ under certain driving amplitude E_ω but showing different collapse positions. Compared with the sinusoidal case,

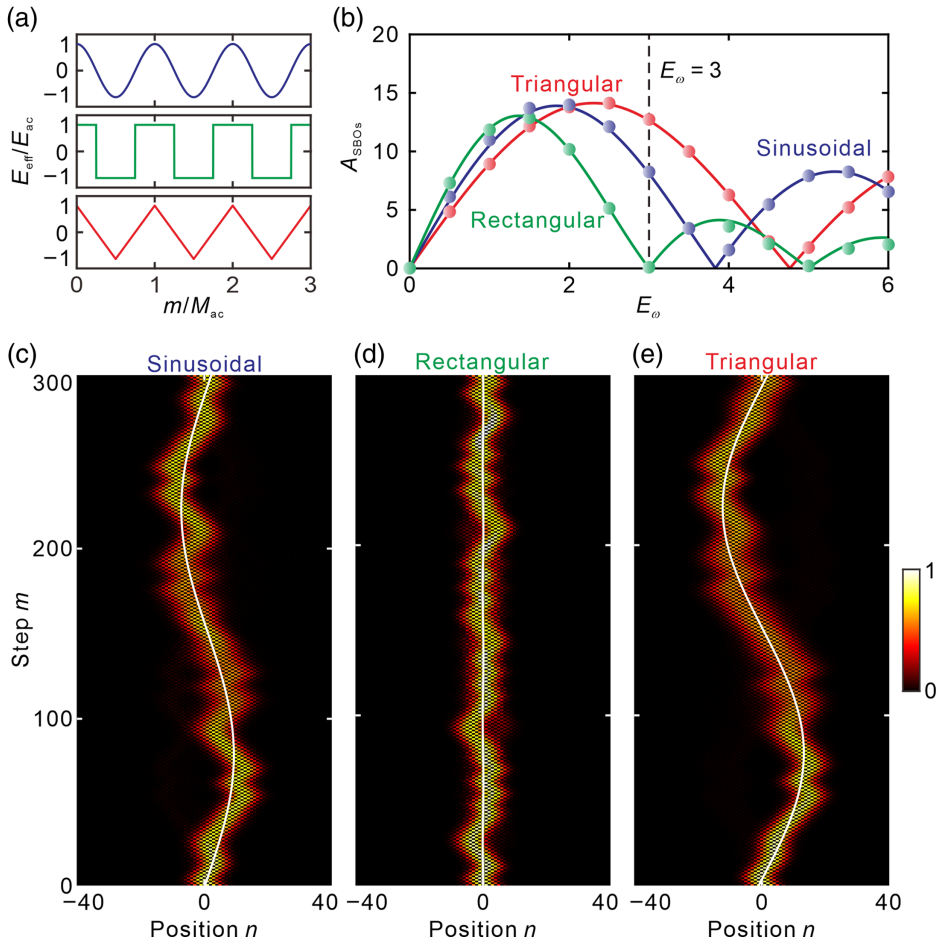

Fig. 5 Generalized SBOs under arbitrary-wave ac-driving fields. (a) Schematic of the sinusoidal-, rectangular-, and triangular-wave ac-driving electric fields. (b) SBO oscillation amplitude $A_{\rm SBOs}$ versus the ac-driving amplitude E_ω under the sinusoidal-, rectangular-, and triangular-wave driving. The solid curves and spheres denote the theoretical and experimental results, respectively. (c)–(e) Measured pulse intensity evolutions under sinusoidal-, rectangular-, and triangular-wave driving, respectively. The ac-driving amplitude is taken as the collapse point for the rectangular-wave driving of $E_\omega = 3$.

the rectangular- and triangular-driving waveforms can achieve SBO collapses at weaker and stronger driving amplitudes. In Figs. 5(c)–5(e), we display the measured packet evolutions for the three cases by choosing the first collapse point of $E_\omega = 3$ for the rectangular-wave case. One can see that $A_{\rm SBOs}$ only vanish for rectangular-wave driving but are nonzero with $A_{\rm SBOs} = 12.6$ and 8.3 for the other two cases, which verifies the above theoretical analysis.

2.4 Applications in Beam Routing and Splitting Using SBO Collapse

In this section, we will exploit the collapse of SBOs to realize the temporal beam routing and splitting applications. Figure 6(a) shows the theoretical and measured packet oscillation displacements $\langle \Delta n_\pm(m) \rangle$ as a function of the driving amplitude E_ω for upper and lower band excitations, which exhibit the flip of oscillation directions by crossing the collapse point of SBOs at $E_\omega = 3.8$. To achieve beam routing, we just need to switch between these collapse points by choosing a weaker or stronger driving amplitude. As depicted in Figs. 6(b) and 6(c), by choosing $E_\omega = 1.8$ and $E_\omega = 5.3$ and exciting only from the upper band at $k = \pi/2$, we can achieve the rightward and leftward beam routing with $\langle \Delta n_\pm(m) \rangle > 0$ and $\langle \Delta n_\pm(m) \rangle < 0$, respectively. The routing directions can also be exchanged by exciting from the lower band. Furthermore, if we simultaneously excite the upper and lower bands, we can also realize the temporal beam splitting. Figures 6(d) and 6(e) show the measured beam evolutions for the case of $E_\omega = 1.8$ and $E_\omega = 5.3$, where the excitation power ratio of upper and lower bands is fixed at 65/35. Interestingly, the power ratios of the two split beams can be switched with each other by switching between weak- and strong-driving regimes to cross the collapse point.

3 Conclusion

We have experimentally demonstrated the collapse of SBOs in the strong-driving regime based on a photonic temporal lattice system. For a sinusoidal ac-driving, we have shown that as the amplitude-to-frequency ratio of the ac-driving field takes the root of the first-order Bessel function, the SBO collapse occurs,

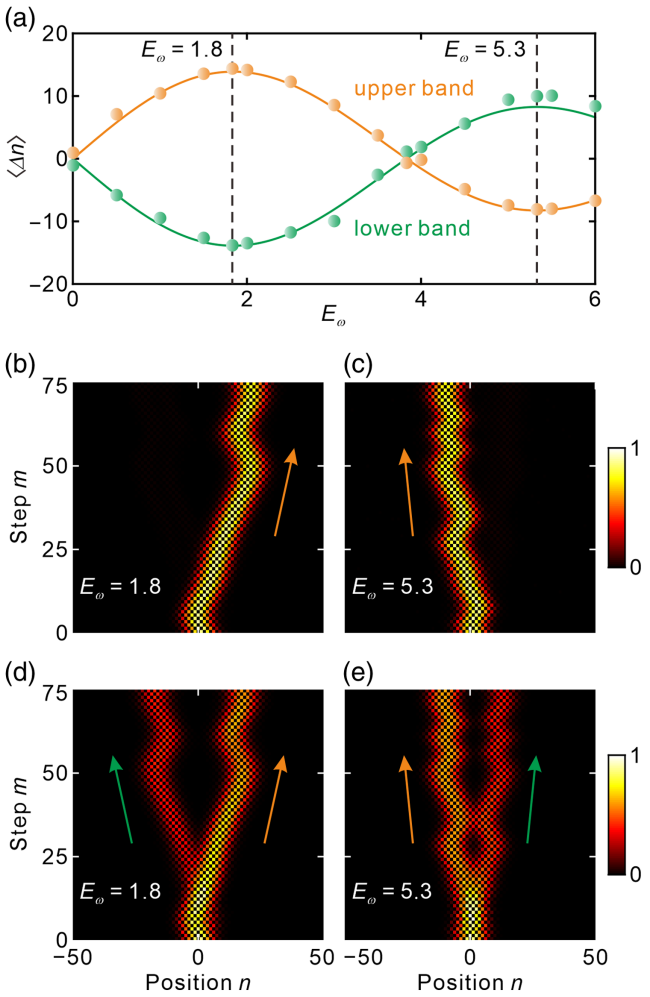

Fig. 6 Application of beam routing and splitting based on SBO collapse. (a) Packet oscillation displacements $\langle \Delta n_{\pm}(m) \rangle$ as a function of the driving amplitude E_ω for upper and lower band excitations. The solid curves and spheres represent the theoretical and experimental results, respectively. (b), (c) Measured pulse intensity evolutions for the upper band excitation at $E_\omega =$ 1.8 and 5.3, respectively. (d), (e) Measured pulse intensity evolutions for the simultaneous excitation of upper and lower bands with the power ratio of 65/35 under the ac-driving amplitudes of $E_\omega = 1.8$ and 5.3, respectively.

manifesting as a complete inhibition of oscillation with a vanishing oscillation amplitude as well as the flip of the initial oscillation direction by crossing the collapse point. Fourier analysis for the instantaneous oscillation trajectory was performed to probe the occurrence of SBO collapse. By replacing the sinusoidal ac-driving with arbitrary-wave ac-driving fields, we also achieved generalized SBOs, which possess different renormalization factors for the oscillation amplitude and hence the distinct collapse conditions. Finally, by switching the driving amplitude between SBO collapse points, we demonstrated experimentally the rightward and leftward beam routing. Thanks to the dual-band nature of the temporal mesh lattice, the temporal beam splitting functionality was also demonstrated by the multiband excitation of the lattice. Our work reported on the first experimental observation of SBO collapse and extended SBOs to the arbitrary-wave ac-driving situations. This paradigm may find potential applications in temporal pulse reshaping and coherent oscillation control for optical communications and signal processing.

Disclosures

The authors declare no competing interests.

Code and Data Availability

Data underlying the results presented in this paper may be obtained from the authors upon reasonable request.

Acknowledgments

The work was supported by the National Natural Science Foundation of China (Grant Nos. 12374305, 12204185, 11974124, 62305122, 62375097, and 12021004), the Natural Science Foundation of Hubei Province (Grant Nos. 2022CFB036 and 2023AFB822), and the Hubei Key Laboratory of Optical Information and Pattern Recognition, Wuhan Institute of Technology (Grant No. 202202).

References

1. J. B. Krieger et al., "Time evolution of Bloch electrons in a homogeneous electric field," *Phys. Rev. B* **33**, 5494–5500 (1986).
2. K. C. Nowack et al., "Coherent control of a single electron spin with electric fields," *Science* **318**, 1430–1433 (2007).
3. H. Lignier et al., "Dynamical control of matter-wave tunneling in periodic potentials," *Phys. Rev. Lett.* **99**, 220403 (2007).
4. C. Waschke et al., "Coherent submillimeter-wave emission from Bloch oscillations in a semiconductor superlattice," *Phys. Rev. Lett.* **70**, 3319–3322 (1993).
5. T. Hartmann et al., "Dynamics of Bloch oscillations," *New J. Phys.* **6**, 2 (2004).
6. C. Qin et al., "Discrete diffraction and Bloch oscillations in non-Hermitian frequency lattices induced by complex photonic gauge fields," *Phys. Rev. B* **101**, 064303 (2020).
7. N. H. Shon et al., "On the dynamic localization in 1D tight-binding systems," *J. Phys.: Condens. Matter* **4**, L611 (1992).
8. N. H. Shon et al., "Dynamic localization of acoustic waves in superlattices," *Phys. Rev. Lett.* **71**, 2935–2938 (1993).
9. J. Wan et al., "Dynamic localization and quasi-Bloch oscillations in general periodic ac-dc electric fields," *Phys. Rev. B* **70**, 125311 (2004).
10. E. Haller, et al., "Inducing transport in a dissipation-free lattice with super Bloch oscillations," *Phys. Rev. Lett.* **104**, 200403 (2010).
11. R. A. Caetano et al., "Wave packet dynamics under superposed DC and AC fields: super Bloch oscillations, resonant directed motion and delocalization," *Phys. Lett. A* **375**, 2770–2774 (2011).
12. K. Kudo et al., "Theoretical analysis of super-Bloch oscillations," *Phys. Rev. A* **83**, 053627 (2011).
13. C. Herrero-Gómez et al., "Super Bloch oscillations in the Peyrard-Bishop-Holstein model," *Phys. Rev. A* **376**, 555–558 (2012).
14. S. Longhi et al., "Correlated super-Bloch oscillations," *Phys. Rev. B* **86**, 075143 (2012).
15. E. Díaz et al., "Super-Bloch oscillations with modulated interaction," *Phys. Rev. A* **87**, 015601 (2013).
16. Z. Turker et al., "Super Bloch oscillation in a PT symmetric system," *Phys. Rev. A* **380**, 2260–2264 (2016).
17. Z. A. Geiger et al., "Observation and uses of position-space Bloch oscillations in an ultracold gas," *Phys. Rev. Lett.* **120**, 213201 (2018).

18. C. Qin et al., "Effective electric-field force for a photon in a synthetic frequency lattice created in a waveguide modulator," *Phys. Rev. A* **97**, 063838 (2018).
19. Z. Huang et al., "Transient dynamics of super Bloch oscillations of a 1D Holstein Polaron under the influence of an external AC electric field," *Ann. Phys.* **531**, 1800303 (2019).
20. A. Cao et al., "Transport controlled by Poincaré orbit topology in a driven inhomogeneous lattice gas," *Phys. Rev. Res.* **2**, 032032 (2020).
21. F. S. Passos et al., "From super-Bloch oscillations to sudden self-trapping in Bose–Einstein condensates with inter-atomic interactions," *Nonlinear Dyn.* **102**, 329–337 (2020).
22. U. Ali et al., "Super-Bloch oscillations with parametric modulation of a parabolic trap," arXiv:2204.12134 (2022).
23. S. X. Xiao et al., "Rabi spectroscopy of super-Bloch oscillations in optical lattice clock," arXiv:2307.11995 (2023).
24. L. Yuan et al., "Photonic gauge potential in a system with a synthetic frequency dimension," *Opt. Lett.* **41**, 741–744 (2016).
25. C. Qin et al., "Spectrum control through discrete frequency diffraction in the presence of photonic gauge potentials," *Phys. Rev. Lett.* **120**, 133901 (2018).
26. K. Wang et al., "Topological complex-energy braiding of non-Hermitian bands," *Nature* **598**, 59–64 (2021).
27. L. Zheng et al., "Chiral Zener tunneling in non-Hermitian frequency lattices," *Opt. Lett.* **47**, 4644–4647 (2022).
28. H. Huang et al., "Experimental observation of the spectral self-imaging effect with a four-wave mixing time lens," *Opt. Lett.* **48**, 1522–1525 (2023).
29. A. Senanian et al., "Programmable large-scale simulation of Bosonic transport in optical synthetic frequency lattices," *Nat. Phys.* **19**, 1333–1339 (2023).
30. A. Regensburger et al., "Photon propagation in a discrete fiber network: an interplay of coherence and losses," *Phys. Rev. Lett.* **107**, 233902 (2011).
31. M. A. Miri et al., "Optical mesh lattices with PT symmetry," *Phys. Rev. A* **86**, 023807 (2012).
32. A. Regensburger et al., "Parity-time synthetic photonic lattices," *Nature* **488**, 167–171 (2012).
33. A. Regensburger et al., "Observation of defect states in PT-symmetric optical lattices," *Phys. Rev. Lett.* **110**, 223902 (2013).
34. M. Wimmer et al., "Optical diametric drive acceleration through action-reaction symmetry breaking," *Nat. Phys.* **9**, 780–784 (2013).
35. M. Wimmer et al., "Experimental measurement of the Berry curvature from anomalous transport," *Nat. Phys.* **13**, 545–550 (2017).
36. S. Wang et al., "PT-symmetric Talbot effect in a temporal mesh lattice," *Phys. Rev. A* **98**, 043832 (2018).
37. S. Weidemann et al., "Topological funneling of light," *Science* **368**, 311–314 (2020).
38. A. Steinfurth et al., "Observation of photonic constant-intensity waves and induced transparency in tailored non-Hermitian lattices," *Sci. Adv.* **8**, eabl7412 (2022).
39. S. Wang et al., "High-order dynamic localization and tunable temporal cloaking in ac-electric-field driven synthetic lattices," *Nat. Commun.* **13**, 7653 (2022).
40. S. Weidemann et al., "Topological triple phase transition in non-Hermitian Floquet quasicrystals," *Nature* **601**, 354–359 (2022).
41. L. Yuan et al., "Temporal modulation brings metamaterials into new era," *Light Sci. Appl.* **11**, 173 (2022).
42. S. Wang et al., "Photonic Floquet Landau-Zener tunneling and temporal beam splitters," *Sci. Adv.* **9**, eadh0415 (2023).
43. H. Ye et al., "Reconfigurable refraction manipulation at synthetic temporal interfaces with scalar and vector gauge potentials," *Proc. Natl. Acad. Sci. U. S. A.* **120**, e2300860120 (2023).
44. H. Ye et al., "Observation of generalized dynamic localizations in arbitrary-wave driven synthetic temporal lattices," *Laser Photonics Rev.* **17**, 2200505 (2023).
45. F. Cardano et al., "Detection of Zak phases and topological invariants in a chiral quantum walk of twisted photons," *Nat. Commun.* **8**, 15516 (2017).
46. X. W. Luo et al., "Synthetic-lattice enabled all-optical devices based on orbital angular momentum of light," *Nat. Commun.* **8**, 16097 (2017).
47. L. Yuan et al., "Synthetic dimension in photonics," *Optica* **5**, 1396–1405 (2018).
48. Y. Song et al., "Two-dimensional non-Hermitian skin effect in a synthetic photonic lattice," *Phys. Rev. Appl.* **14**, 064076 (2020).
49. K. Fang et al., "Photonic Aharonov-Bohm effect based on dynamic modulation," *Phys. Rev. Lett.* **108**, 153901 (2012).
50. Q. Lin et al., "Light guiding by effective gauge field for photons," *Phys. Rev. X* **4**, 031031 (2014).

Xinyuan Hu received her BS degree from the School of Physics, Jilin University, China, in 2020. She is currently a PhD student at Huazhong University of Science and Technology, Wuhan, China. Her research interests focus on deep learning and nanophotonics.

Shulin Wang received his PhD from the School of Physics, Huazhong University of Science and Technology, Wuhan, China, in 2021. He is currently a postdoctoral fellow at Wuhan National Laboratory for Optoelectronics, Huazhong University of Science and Technology. His current research interests include synthetic dimensions, non-Hermitian physics, and nonlinear optics.

Chengzhi Qin received his BS degree in optics and electronic information and his PhD in physics from Huazhong University of Science and Technology, Wuhan, China, in 2014 and 2019, respectively. He is currently an associate professor at the School of Physics, Huazhong University of Science and Technology. His research interests include topological photonics, nanophotonics, and non-Hermitian physics.

Chenyu Liu received her BS degree from the School of Physics, Huazhong University of Science and Technology, China, in 2021. She is currently a PhD student at Huazhong University of Science and Technology. Her research interests focus on synthetic dimensions and nonlinear optics.

Lange Zhao received her BS degree from the School of Physics, Huazhong University of Science and Technology, China, in 2019. She is currently a PhD student at Huazhong University of Science and Technology. Her research interests focus on nanophotonics and non-Hermitian physics.

Yinglan Li received his BS degree from China Three Gorges University, China, in 2022. He is currently a PhD student at Huazhong University of Science and Technology. His research interests focus on nanophotonics and non-Hermitian physics.

Han Ye received his BS and PhD degrees from the School of Physics, Huazhong University of Science and Technology, China, in 2018 and 2023, respectively. His research interests focus on nanophotonics and non-Hermitian physics.

Weiwei Liu received his BS and PhD degrees in optics and electronic information both from Huazhong University of Science and Technology, Wuhan, China, in 2012 and 2017, respectively. He is currently an associate professor at the School of Physics, Huazhong University of Science and Technology. His research interests include nonlinear optics, nanophotonics, and topological photonics.

Stefano Longhi received his PhD degree in physics from the Polytechnic Institute of Turin (with distinguished honor) in 1996. He is currently a

full professor in the Physics Department, Polytechnic Institute of Milan, and a research associate at IFISC, University of the Balearic Islands, Palma de Mallorca (Spain). His research interests include photonics, quantum optics, and non-Hermitian physics.

Peixiang Lu received his PhD from the Shanghai Institute of Optics and Fine Mechanics, Chinese Academy of Sciences, Shanghai, in 1992. He is currently a professor at Wuhan National Laboratory for Optoelectronics, Huazhong University of Science and Technology. He is a fellow of the Optical Society of America. His current research interests include ultrafast optics, laser physics, and nanophotonics.

Bing Wang received his BS and PhD degrees in physics from Wuhan University, Wuhan, China in 2002 and 2007, respectively. He is currently a professor at the School of Physics and Wuhan National Laboratory for Optoelectronics, Huazhong University of Science and Technology, Wuhan, China. His research interests include metal/graphene plasmonics, nanophotonics, nonlinear, and ultrafast optics.